Engineering Geology 303 (2022) 106651

Contents lists available at ScienceDirect

Engineering Geology

journal homepage: www.elsevier.com/locate/enggeo

Roof stability in flat-ceiling deep rock cavities and tunnels

Dowon Park [a], Radoslaw L. Michalowski [b,*]

[a] Department of Civil Engineering, University of Seoul, 163 Seoulsiripdae-ro, Dongdaemun-gu, Seoul 02504, South Korea
[b] Department of Civil & Environmental Engineering, University of Michigan, 2028 G.G. Brown Bldg., Ann Arbor, MI 48109-2125, USA

ARTICLE INFO

Keywords:
Rock cavity
Tunnels
Roof rock stability
Hoek-Brown criterion
Quadric block
Quartic conical block

ABSTRACT

Three-dimensional stability of roofs in deep flat-ceiling cavities is analyzed. The stability number, factor of safety, and required supporting stress are used as measures of roof stability. Despite the simplicity of the flat roof geometry, the three-dimensional stability analysis presents some complexities owed to the shape of the failure surface geometry in the collapse mechanism. The failure mode assumes a rock block moving downward into the cavity, and the study aims to recognize the most critical shape of the failing block. Three specific block shapes are described in some detail, but more have been analyzed. Blocks defined by a special case of a 4th order conical surface (quartic) on a rectangular base, and a 2nd order elliptic surface (quadric) are found to be the most critical in the stability analysis. The kinematic approach of limit analysis was used, with the rock strength governed by the Hoek-Brown failure criterion. The parametric form of the Hoek-Brown function was employed. Interestingly, an absence of diagonal symmetries in the most critical failure mechanisms was observed in roof collapse of square-ceiling cavities. Computational results in terms of dimensionless measures of stability are presented in charts and tables.

1. Introduction

With an increasing use of underground space for transportation, commercial and sport facilities, as well as for storage and waste disposal, the subject of cavity roof stability appears to be important, yet not systematically explored. An early investigation into roof stability in the context of tunnels was carried out by Lippmann (1971), who employed both the kinematic and static approaches of limit analysis. In that study, a rectangular tunnel in rock with strength governed by the Mohr-Coulomb failure criterion was considered. Since then, 2D (Fraldi and Guarracino, 2009, 2010; Leca and Dormieux, 1990; Park and Michalowski, 2018, 2019; Sloan and Assadi, 1992; Suchowerska et al., 2012) and 3D (Huang et al., 2014; Park and Michalowski, 2020; Yang and Huang, 2013) stability analyses of cavity or tunnel roofs have been carried out.

Some of the 2D analyses used a variational approach (Fraldi and Guarracino, 2009, 2010), but the advancement of this approach to 3D analyses is hindered by mathematical complexity (with the exception of axial symmetry). They also have focused mostly on finding profiles of failing blocks, and not the results in terms of stability measures. Some of these limitations have been overcome by applying analytical techniques (Park and Michalowski, 2019, 2020), yet 3D stability analyses of flat-ceiling cavities have not been addressed beyond special cases, such as axial symmetry. A right elliptic cone block mechanism adopted for cylindrical cavities such as tunnels (Park and Michalowski, 2020) may be applicable to flat-ceiling cavities, but the expectation that the base of the failing block should be elliptic (or circular) is rather arbitrary for cavities with rectangular ceilings. One should expect that the critical failure mechanism of a flat rectangular-ceiling cavity would include the entire rectangular surface of the ceiling, but finding a collapse mechanism that includes the four corners of the cavity poses additional challenges.

Three plausible shapes of failing blocks are described in this study with some detail. Among them a special case of the 4th order surface (quartic) cone block on a rectangular base is considered, which allows the construction of an admissible failure mechanism that includes the entire ceiling of the cavity. Despite the complexity of the failing block shape, the analysis carried out makes it possible to calculate the stability measures of the roof. Blocks defined by 2nd order surfaces (quadrics) and pyramid-type blocks were also studied. Three additional quartic surfaces were analyzed, but these are only briefly mentioned in the penultimate section.

The kinematic approach of limit analysis is used in the study, and the parametric form of the Hoek-Brown failure criterion is used to facilitate calculations of the rate of dissipated work in the analysis. This approach

* Corresponding author.
E-mail address: rlmich@umich.edu (R.L. Michalowski).

https://doi.org/10.1016/j.enggeo.2022.106651
Received 1 August 2021; Received in revised form 25 March 2022; Accepted 29 March 2022
Available online 2 April 2022

was developed earlier by the authors and it was applied in both the tunnel and slope stability analyses (Park and Michalowski, 2019, 2020, 2021; Michalowski and Park, 2020).

A brief review of the Hoek-Brown failure criterion is presented in Section 2. Next, the method of analysis and the stability measures are summarized, followed by the problem description, all in Section 3. Construction of failure mechanisms is illustrated in Section 4. Numerical results are presented in Section 5, with attention paid to some peculiarities in the outcome. The conclusions are presented in Section 6.

2. Hoek-Brown failure criterion for rocks

Nonlinear pressure dependency of the peak strength of rock has made it complicated to find a convenient form of strength criteria for rocks. Among various failure envelopes suggested for rock mass (Barton, 1976; Bieniawski, 1974; Hoek and Brown, 1980; Paul, 1961), the Hoek-Brown criterion has been widely accepted in rock mechanics and engineering. The advantage of the Hoek-Brown criterion over alternatives is in its direct link to geological observations assessing the rock type, quality, and disturbance, which give rise to the model parameters and indices. This criterion considers the strength of intact rock, and its strength is reduced based on observations of disturbance and weathering, to predict a more realistic rock mass behavior. In recent decades this criterion has been modified, with the last updates in 2002 (Hoek et al., 2002), summarized in 2007 (Hoek and Marinos, 2007), and Hoek and Brown (2019).

The generalized Hoek-Brown failure criterion (Hoek and Brown, 2019; Hoek et al., 2002) is written as

$$\sigma_1' = \sigma_3' + \sigma_{ci}\left(m_b\frac{\sigma_3'}{\sigma_{ci}} + s\right)^a \tag{1}$$

where σ_1' and σ_3' are the major and minor effective principal stresses at failure, respectively; σ_{ci} is the uniaxial compressive strength of the intact rock. The criterion in Eq. (1) is graphically presented in Fig. 1. Dimensionless parameters m_b, a, and s are defined as follows

$$m_b = m_i e^{\left(\frac{GSI-100}{28-14D}\right)} \tag{2}$$

$$a = \frac{1}{2} + \frac{1}{6}\left(e^{-\frac{GSI}{15}} - e^{-\frac{20}{3}}\right) \tag{3}$$

$$s = e^{\left(\frac{GSI-100}{9-3D}\right)} \tag{4}$$

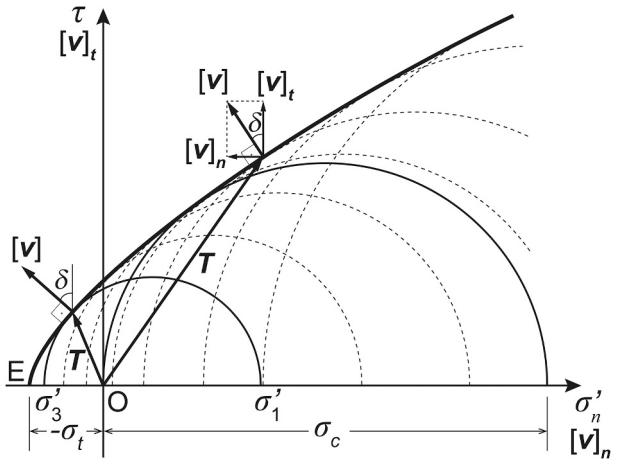

Fig. 1. The Hoek-Brown failure criterion in $\tau - \sigma_n'$ plane.

where m_i is the rock type-dependent parameter (varying generally between 5 and 30), D is the disturbance factor (0–1, 0 for minimally disturbed and 1 for very disturbed rock masses), and GSI is the Geological Strength Index (5–100). The uniaxial compressive strength of the rock can be found by substituting $\sigma_3' = 0$ and $\sigma_1' = \sigma_c$ into Eq. (1)

$$\sigma_c = \sigma_{ci} s^a \tag{5}$$

Hoek et al. (2002) suggested that uniaxial tensile strength σ_t be found by setting $\sigma_1' = \sigma_3' = -\sigma_t$ in Eq. (1), as the difference between the uniaxial and isotropic tensile strength is often negligible for brittle materials. The isotropic tensile strength of rock corresponds to point E in Fig. 1, and reads

$$\sigma_t = \frac{s\sigma_{ci}}{m_b} \tag{6}$$

Hereafter, the prime corresponding to the effective stress will be omitted. The Hoek-Brown failure criterion is an explicit function of the major and minor principal stresses, whereas plotting it on the stress plane in Fig. 1 requires the shear strength as a function of the normal stress. Using an earlier development of Balmer (1952) it is possible to represent the criterion in Eq. (1) in the following parametric form (Kumar, 1998)

$$\sigma_n' = \sigma_{ci}\left\{\left(\frac{1}{m_b} + \frac{sin\delta}{m_b a}\right)\left[\frac{m_b a(1-sin\delta)}{2sin\delta}\right]^{\frac{1}{1-a}} - \frac{s}{m_b}\right\} \tag{7}$$

$$\tau = \sigma_{ci}\left\{\frac{cos\delta}{2}\left[\frac{m_b a(1-sin\delta)}{2sin\delta}\right]^{\frac{a}{1-a}}\right\} \tag{8}$$

where angle δ is the shear or the rupture angle illustrated in Fig. 1. This parametric form of the Hoek-Brown failure criterion is instrumental in the stability analysis carried out in this study.

3. Analysis method and problem description

3.1. Method of analysis

The kinematic approach of limit analysis is employed to obtain stability measures, which determine the safety of flat-ceiling roofs over deep cavities or tunnels. Deep cavities are defined as those for which a potential failure mechanism does not propagate to the ground surface. Application of the theorems of limit analysis requires that the material deforms plastically, while rocks have a tendency to fracture, particularly at low confining stresses. However, Chen (1975) argued that small irreversible strain observed in rocks prior to brittle stress drop-off may allow application of plasticity theorems in rocks. This is why one can find earlier applications of limit theorems in rock analyses (Chen and Drucker, 1969; Lippmann, 1971; Michalowski, 1985). The kinematic theorem of limit analysis can be written as

$$\int_L T_i\,[v]_i\,dL \;\geq\; \int_V X_i v_i\,dV + \int_S p_i v_i\,dS \tag{9}$$

with the left side being the rate of internal (dissipated) work on failure surfaces L, and the right side is the sum of the external forces work rate: distributed forces X_i in mechanism volume V and boundary stress p_i on boundary S. The rate of dissipated work in any kinematically admissible mechanism is not less than the work rate of true external forces. The use of inequality (9) employs the balance of internal and external work rates

$$D = W_\gamma + W_p \tag{10}$$

The three terms in the balance Eq. (10) correspond to the three terms in inequality (9). Eq. (10) leads to an upper bound for the active load causing failure of a structure (Drucker et al., 1952). However, the outcome of the work rate balance can be formulated in terms of rigorous

bounds to other stability measures, such as the factor of safety or a stability number, which is explored in this paper.

Applicability of the theorem requires that the strength of the material conforms to a convex strength envelope and the incipient failure mechanism is characterized by plastic (ductile) deformation governed by the normality flow rule.

The failure mechanisms considered in this paper consist of a rigid block separated from the rock at rest by rupture bands interpreted as failure surfaces. The velocity discontinuity vector $[v]_i$ on those surfaces is defined by the normality flow rule, as illustrated in Fig. 1. Angle δ is referred to as the *rupture angle*; for more details, see Michalowski and Park (2020) and Park and Michalowski (2017).

3.2. Measures of safety assessment

Three measures of roof stability are examined: stability number, factor of safety, and supporting pressure required to prevent roof failure. Stability number N has been traditionally used in assessment of slope safety (Taylor, 1937), where it is defined as a dimensionless group including soil properties and slope geometry. To define a similar quantitative measure to express the limit state of cavities in rock, we chose the following expression

$$N = \left(\frac{\sigma_{ci}}{\gamma B}\right)_{crit} \tag{11}$$

with σ_{ci} and γ being the uniaxial compressive strength and the unit weight of intact rock, respectively, and B is the cavity width. The stability number in Eq. (11) is a critical combination of dimensionless group $\sigma_{ci}/\gamma B$, characterizing the instant of failure. Every cavity or tunnel can be characterized by group $\sigma_{ci}/\gamma B$, and one can identify the margin of safety by the difference of its value and the value of the stability number. Combinations $\sigma_{ci}/\gamma B$ larger than stability number N define a stable roof, and the larger the difference the larger the safety margin. The failure state is reached when dimensionless group $\sigma_{ci}/\gamma B$ drops to the value of stability number N.

Factor of safety F is defined by the ratio of shear strength τ of the rock to the demand on shear strength τ_d required for limit equilibrium (an instant of impending failure)

$$F = \frac{\tau}{\tau_d} \tag{12}$$

The factor of safety based on the shear strength shown in Eq. (12) is commonly used in geotechnical engineering for characterizing stability of earth structures. An application of this definition to geomaterials governed by failure criteria with linear dependence on the mean stress is fairly straightforward. For rocks, where this dependence is non-linear the application is cumbersome, and for the Hoek-Brown criterion, which is defined as a function of principal stresses, it is particularly intricate. For that reason, the factor of safety for rock structures is often taken as a function of the factored uniaxial compressive strength rather than shear strength, e.g., Li et al. (2008). In problems such as stability of slopes, the factor of safety so formulated appears to grossly overestimate the factor based on the shear strength (Michalowski and Park, 2020). However, for flat-ceiling roof collapse the two become identical, which is something of a peculiarity.

The third measure of roof stability considered here is supporting pressure p, defined as the minimum of a uniformly distributed pressure on the cavity ceiling needed to assure a target factor of safety. The dimensionless form $p/\gamma B$ is examined in this paper. This pressure is a reaction of the tunnel lining or a structural support in underground cavities.

3.3. Problem description

This study investigates roof stability in flat-ceiling cavities and tunnels at a depth preventing the collapse mechanism from propagating to the ground surface. The strength of the surrounding rock is governed by the Hoek-Brown failure criterion, and the rock is uniform, without distinct joints that might skew the collapse pattern. The cavities analyzed have rectangular (or square) ceilings, which determine the maximum possible extent of the roof collapse mechanism. In the case of tunnels, the length of the cavity is defined by the spacing of the periodic structural ribs. Calculations indicated that critical collapse mechanisms, in all cases considered, reached the maximum size allowable by the dimensions of the ceiling. This is likely because during failure the work is dissipated along rupture surfaces and it increases with the square of the cavity size, whereas the work of the weight, which causes the failure, increases with the cube of the size of the mechanism.

The surfaces in Fig. 2 illustrate the blocks considered in the failure mechanisms. Each of the blocks contains a prismatic central part and the end sections formed by two symmetric halves of a right cone (Fig. 2(a, b)) or a pyramid (Fig. 2(c)). All components within each block move with uniform downward velocity, forming a rigid block, with the work dissipated during failure only on the rupture surface between the moving block and the stationary rock above. The cone sections in Figs. 2 (a) and 2(b) are constructed of a series of conical frusta derived from a special case of quartic cones, and elliptic (quadric) cones, respectively. All mechanisms reach the maximum base size determined by the size of the cavity ceiling, as discussed in the previous paragraph. The blocks in Figs. 2(a) and 2(c) cover the entire ceiling of the cavity, but the one in Fig. 2(b) does not reach into the corners, as it is constrained by the elliptic base. The results will be presented as dimensionless numbers, applicable to any size of the cavity ceiling.

The mechanism of the roof failure consists of a rock block (one of the three in Fig. 2), which moves downward into the cavity, driven by the gravity load. Before separating from the rock above, it is assumed that plastic deformation takes place in a narrow zone between the moving block and the stationary rock above. This last assumption makes the plasticity analysis applicable.

4. Analysis of roof collapse in flat-ceiling cavities

4.1. Centric prismatic block with piece-wise linear inclination

All failure blocks considered in Fig. 2 include a central prismatic portion, called also an *insert*. The transverse cross-section of the insert is illustrated in Fig. 3(a), and it is identical to the contours of the adjacent end sections, together forming one integrated block. During collapse, the rock fails along *rupture surface* $B_1B_jB_{n+1}$ (interpreted as a narrow band of plastically deforming material).

Cross-section $B_1B_jB_{n+1}$ of the rupture surface forms a polygon. Describing the geometry of this piece-wise linear cross-section with n segments, one needs to define n angles α_j ($j = 1, 2\ldots n$) and $n-1$ angles η_j; because point O′ is selected at $B/2$ beneath the ceiling, the sum of all angles η_j is equal to 45° (both sets of angles are shown in Fig. 3(a)). The block is symmetric and number n defines the number of segments in one symmetric half ($n = 5$ is shown on the left side of Fig. 3(a) and $n = 10$ on the right side). The accuracy of the analysis increases with an increase in number n, and $n = 10$ was used in all calculations. Angles α_j and η_j will become independent variables in the process of finding the most critical failure block.

During collapse, the blocks shown in Fig. 2 move downward with uniform velocity v. This velocity is marked as [v], along the failure surface, to indicate that it is the velocity discontinuity between the moving block and the rock at rest, but both have the same direction and magnitude. Vector [v] is inclined to the rupture surface at angle δ, which is different for each segment, and is defined as $\delta_j = \pi/2 - \alpha_j$ ($j = 1, 2\ldots n$). Rupture angle δ is uniquely related to a point on the rock strength envelope through the normality flow rule, as illustrated in Fig. 1. In general, with an increase in rupture angle δ, the stress in the rock will change from the compressive to the tensile regime, Fig. 1.

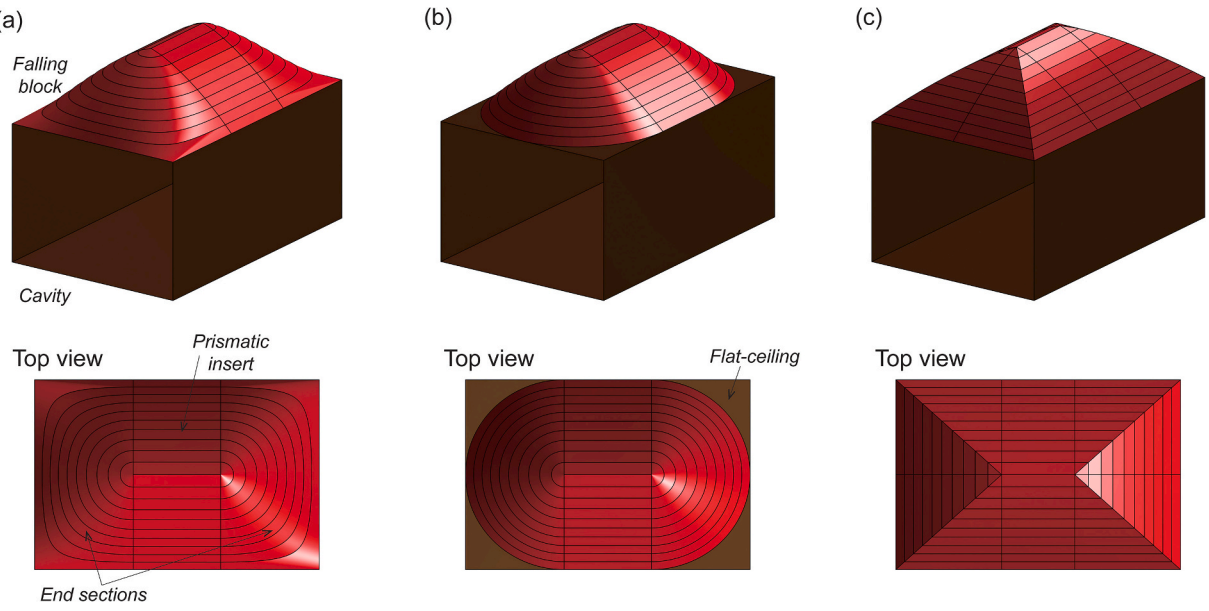

Fig. 2. A schematic of 3D flat-ceiling cavity roof failure blocks: (a) a special case of 4th order (quartic) cone block on rectangular base with a prismatic insert, (b) real quadric (elliptic) cone block with insert, and (c) pyramid-type block with insert. (For interpretation of the references to colour in this figure legend, the reader is referred to the web version of this article.)

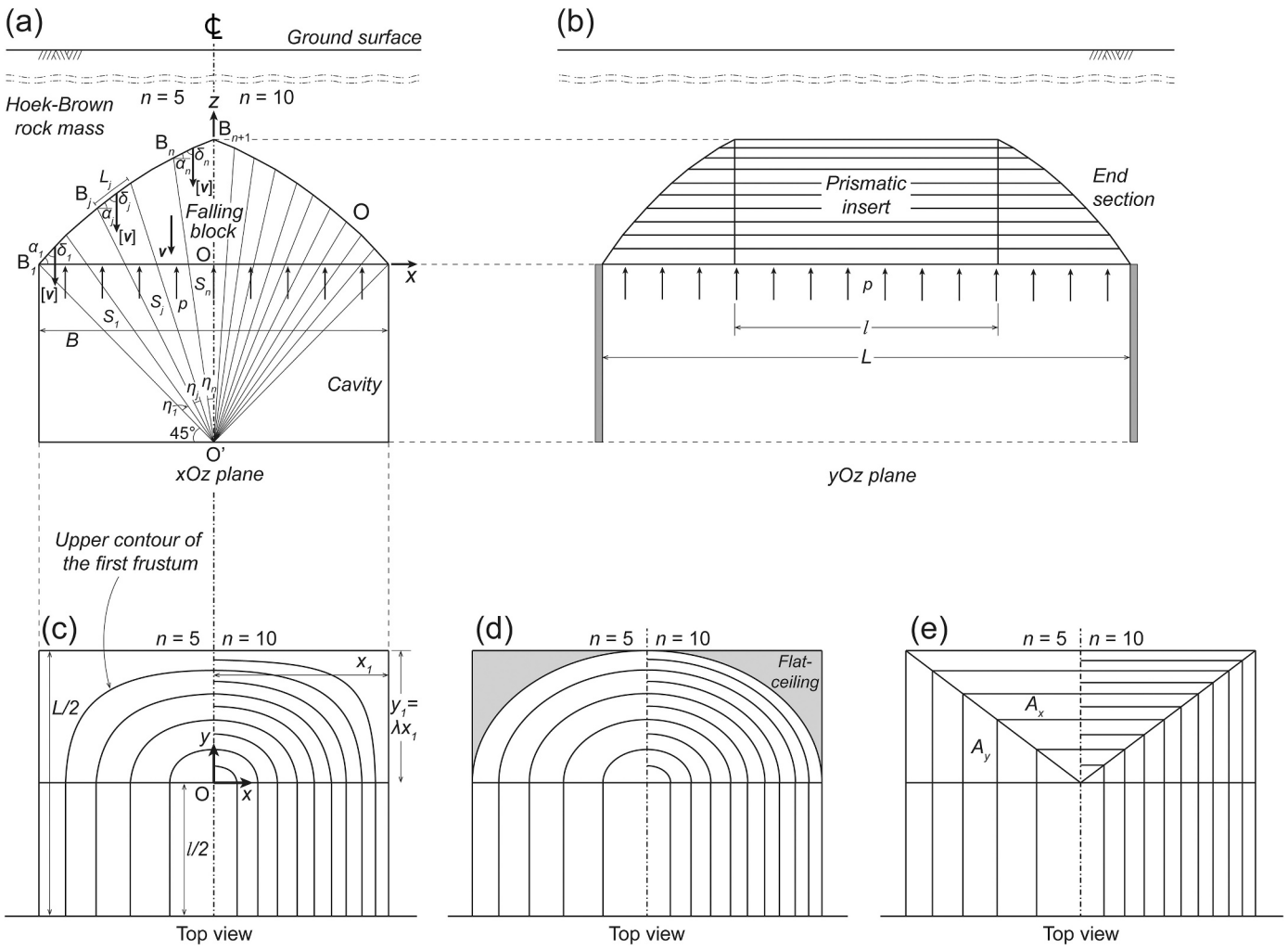

Fig. 3. Geometry of failing blocks in flat-ceiling cavities: (a) transverse cross-section *xOz*, (b) prismatic insert with end sections on longitudinal plane *yOz*, (c) top view of quartic cone block on rectangular base with insert, (d) real quadric (elliptic) cone block with insert, and (e) rectangle-based pyramid with insert.

The rates of the dissipated work and the gravity work in Eq. (10) for the prismatic block insert can be easily determined (for example, following Park and Michalowski (2019)), and they are summarized in Eqs. (A1) through (A3) in Appendix A. The analysis of the central prismatic insert is the same for all three blocks in Fig. 2. In the following, end sections for the three different blocks are analyzed.

4.2. Quartic cone block with rectangular base

Consider a surface defined in the following algebraic equation

$$\frac{x^2}{a^2}+\frac{y^2}{b^2}-\frac{x^2}{a^2}\frac{y^2}{b^2}=\frac{(z-h)^2}{h^2} \tag{13}$$

Without the third term on the left, it represents a classic *right elliptic cone* with height h, also called the *real quadric cone* (surfaces defined by a second-order algebraic equation are called *quadrics*). The coordinate system starts at the base of the cone, with z directed toward the cone apex, as in Fig. 4. The addition of the third term on the left makes this cone have a rectangular base of size $2b \times 2a$, and it becomes a special case of a 4th order cone. This cone has a linear generatrix in planes $x = 0$ and $y = 0$, but nowhere else. We will refer to this special case 4th order cone as the *quartic cone*.

Multiplying Eq. (13) by a^2 and substituting the cone height with z-coordinate c_1 of its apex, this surface can be expressed as

$$x^2+\frac{y^2}{\lambda^2}-\frac{x^2y^2}{(\lambda x_1)^2}=\frac{(z-c_1)^2}{tan^2\alpha_1} \tag{14}$$

where λ is the ratio of half-axes ($\lambda = b/a$), and half-axis a was replaced with magnitude x_1 of coordinate x. The end sections of the block in Fig. 2 (a) and Fig. 3(c) are constructed by n frusta of cones, with the first one defined by Eq. (14), and each consecutive frustum being a part of a cone as in Eq. (14), but with different inclination angle α_j of the generatrix in plane xOz (Fig. 3(a)). In the following, the steps in constructing the entire cone are described.

Rearranging Eq. (14) one can easily represent coordinate z of any point on the surface of the first cone as function $z = f_1(x,y)$

$$f_1(x,y)=c_1-tan\alpha_1\sqrt{x^2+\frac{y^2}{\lambda^2}-\frac{x^2y^2}{(\lambda x_1)^2}} \tag{15}$$

The symmetric half of cross-section $y = 0$ of function $f_1(x,y)$ is shown in Fig. 4(a). This cone will only contribute the bottom-most frustum to the entire failing block, limited by $z_1 \le z < z_2$ ($z_1 = 0$). Coordinates z_j are uniquely determined by independent variables α_j and η_j for the prismatic insert, Fig. 3(a). Next, function $f_2(x,y)$ for the cone contributing the second frustum is derived. Location of point B_2 in Fig. 4(b) is known from the construction of the prismatic portion of the block, Fig. 3(a). The trace of $f_1(x,y)$ on plane $y = 0$ in Fig. 4(a) is rotated clockwise about point B_2 until it reaches inclination angle α_2. Using the geometrical relations in Fig. 4(b), the following expression is derived

$$\begin{aligned} f_2(x,y) &= z_2+[f_1(x,y)-z_2]\frac{tan\alpha_2}{tan\alpha_1} \\ &= z_2+(c_1-z_2)\frac{tan\alpha_2}{tan\alpha_1}-tan\alpha_2\sqrt{x^2+\frac{y^2}{\lambda^2}-\frac{x^2y^2}{(\lambda x_1)^2}} \\ &= c_2-tan\alpha_2\sqrt{x^2+\frac{y^2}{\lambda^2}-\frac{x^2y^2}{(\lambda x_1)^2}} \end{aligned} \tag{16}$$

where $f_2(x,y)$ describes the shape of the second cone, which contributes the second frustum to the entire block, and c_2 is the coordinate of the apex of the second cone, Fig. 4(b). Eq. (16) guarantees continuity of the block surface (but not its derivative) when transitioning from the first frustum to the second. The shape of the consecutive cones j ($j = 2, 3\ldots n$) is determined from

$$\begin{aligned} f_j(x,y) &= z_j+[f_{j-1}(x,y)-z_j]\frac{tan\alpha_j}{tan\alpha_{j-1}} \\ &= c_j-\tan\alpha_j\sqrt{x^2+\frac{y^2}{\lambda^2}-\frac{x^2y^2}{(\lambda x_1)^2}}, \quad z_j \le z \le z_{j+1} \end{aligned} \tag{17}$$

with

$$c_j=(c_{j-1}-z_j)\frac{tan\alpha_j}{tan\alpha_{j-1}}+z_j \tag{18}$$

The sequence of developing the shape of the failing block with $n = 5$ (four frusta and the top cone) is illustrated in Fig. 5, with the bottom row showing the top view of the constructed block. The curved lines illustrate the interfaces between the consecutive frusta. Each consecutive cone j contributes a frustum between coordinates z_j and z_{j+1}. The base of the cone so constructed is a rectangle, but it transitions to an oval cross-section as z increases.

By manipulating Eq. (17), the y-coordinates of the j^{th} elliptic cone can be found from

$$y=\pm\sqrt{\frac{\left(\frac{c_j-z}{tan\alpha_j}\right)^2-x^2}{\frac{1}{\lambda^2}-\frac{x^2}{(\lambda x_1)^2}}} \tag{19}$$

with valid ranges of x and z being $x_j \le x < 0$ and $z_j \le z < z_{j+1}$,

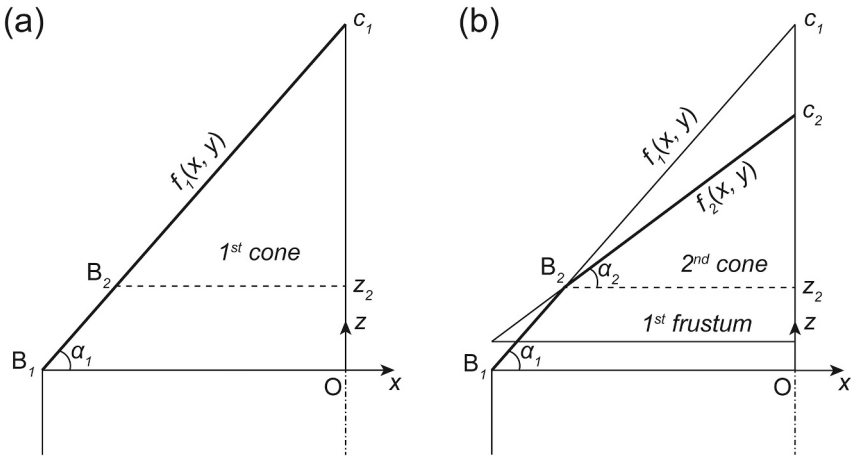

Fig. 4. Construction of functions $f(x,y)$ in plane $y = 0$ (section xOz): (a) the bottom-most frustum defined by function $f_1(x,y)$, and (b) construction of function $f_2(x,y)$ based on $f_1(x,y)$.

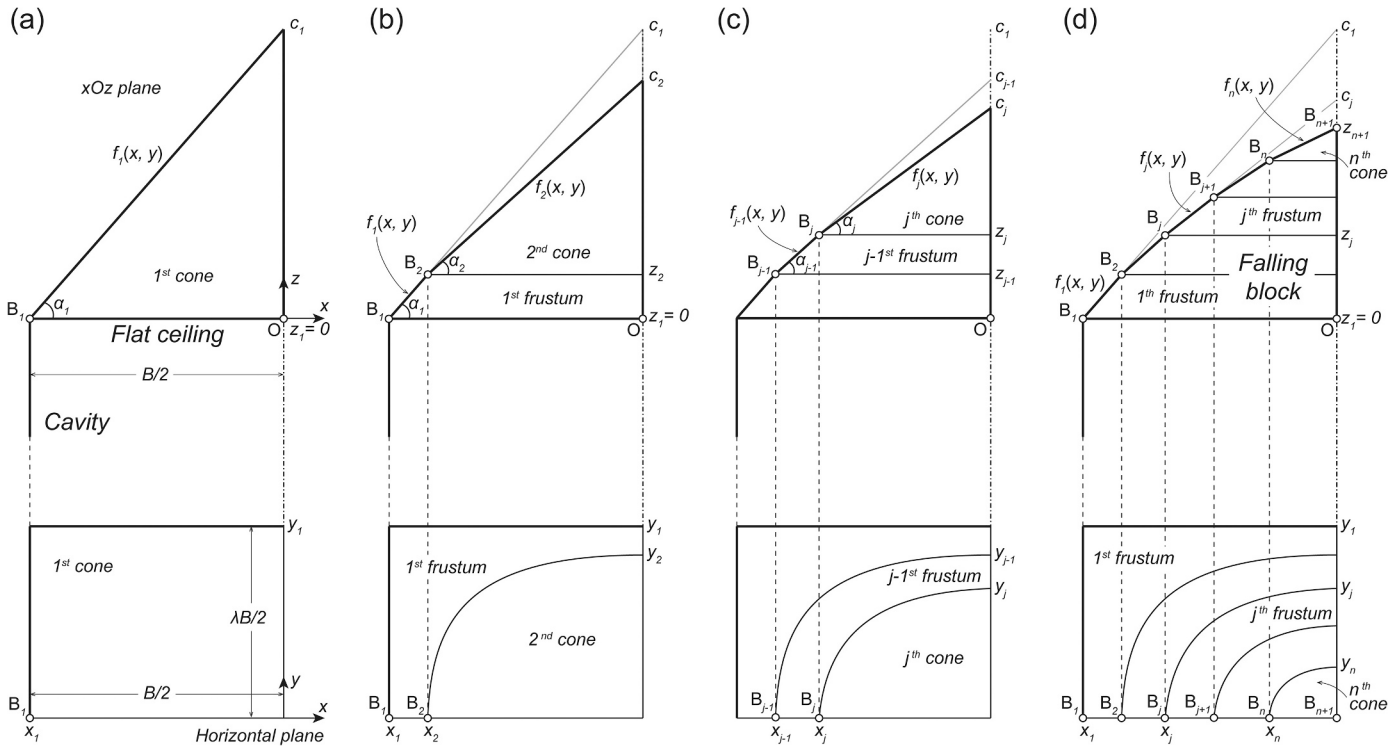

Fig. 5. Constructing one quadrant of the quartic cone block on rectangular base. Upper row: constructing the sequence of frusta. Lower row: top view of constructed block.

respectively. The plus-minus sign indicates the conical surfaces on two sides of the symmetry plane. The equations above fully describe the shape of the cone with a rectangular base, consisting of the frusta of quartic cones.

The geometry of the quartic cone block described above is complex and one might want to use a purely numerical approach to generate a surface with similar properties. Such an attempt was shown by Mollon et al. (2011) in an analysis of a tunnel face stability. Once the rotational failure was adopted, the inclination of an individual element in the constructed failure surface was uniquely determined by the flow rule associated with the Mohr-Coulomb criterion used by Mollon et al. (2011). Such an approach was not used by the authors because of multiplicity of rupture angles involved in the Hoek-Brown failure criterion, leading to a multitude of possible element inclinations. Optimization of such a surface would be impractical. However, the numerical method will be used to carry out calculations of the work rate terms in the analysis.

The complex geometry of the quartic failure surface hinders the analytical formulation of the work rate terms in Eq. (10). The generatrix of the quartic cone block is piece-wise linear (Fig. 5(d)) only in cross-sections *xOz* and *yOz*; therefore, the rupture angle varies on the surface of every frustum contributing to the entire block. Consequently, a purely numerical technique was utilized to estimate the rate of work dissipation and the rate of external work for the end sections of the block. The 3D contour of the failure surface was discretized using the Delaunay triangulation method (Delaunay, 1934), as shown in Fig. 6. The complex shape of the failure surface is discretized into m small triangular elements with y-coordinate of corner points determined by Eq. (19) for given x and z. For each frustum j coordinates x and z are in the range $x_j \le x < 0$ and $z_j \le z < z_{j+1}$. The area of each triangular element is obtained as a half of the magnitude of the vector product $\left|\vec{p}_k \times \vec{q}_k\right|$ ($k = 1, 2 \ldots m$), as illustrated in Fig. 6(b)

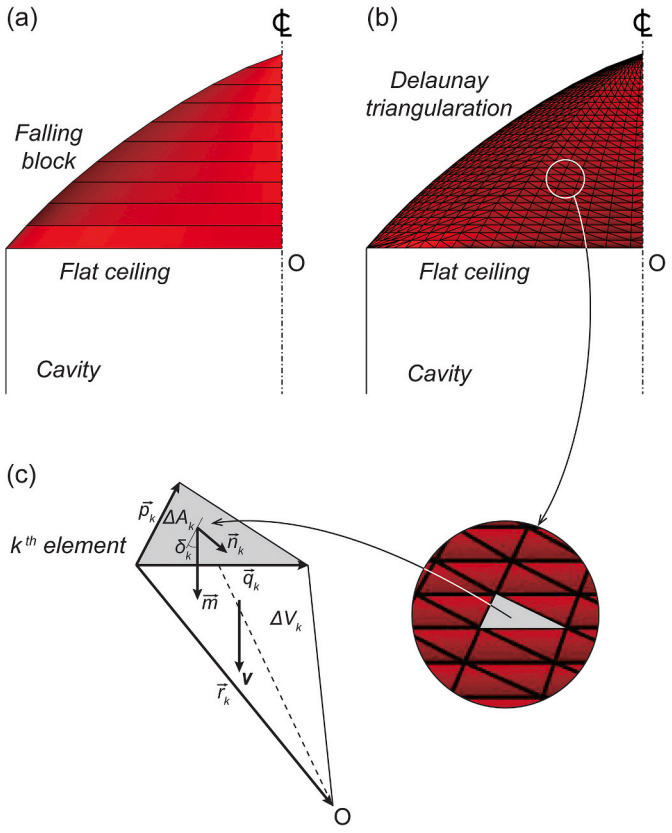

Fig. 6. Delaunay discretization of the block surface: (a) failure block made of conical frusta, (b) discretization using Delaunay triangulation method, and (c) surface element ΔA_k and volume element ΔV_k. (For interpretation of the references to colour in this figure legend, the reader is referred to the web version of this article.)

$$\Delta A_k = \frac{1}{2}\left|\vec{p}_k \times \vec{q}_k\right| \tag{20}$$

Vectors $\vec{p}_k$ and $\vec{q}_k$ are found from the coordinates of the nodal points in the triangulated surface. A vector normal to a triangular element is determined by the cross product

$$\vec{n}_k = \vec{p}_k \times \vec{q}_k \tag{21}$$

and the direction of block velocity vector v is given by unit vector

$$\vec{m} = (0, 0, -1) \tag{22}$$

The normality flow rule enforced in limit analysis requires velocity discontinuity vector [v] on the failure surface (each triangular element) to be inclined at rupture angle δ to that surface, Fig. 6(c). Therefore, rupture angle δ can be found as the complementary angle to the angle between vectors $\vec{n}_k$ and $\vec{m}$

$$\delta_k = \frac{\pi}{2} - cos^{-1}\frac{|\vec{n_k}\cdot\vec{m}|}{\|\vec{n_k}\|\|\vec{m}\|} \tag{23}$$

Because of the two planes of symmetry, only one quarter of the failure surface is analyzed for all conical end sections considered in this paper. The rate of the internal work on one fourth of the failure surface is the sum of the rates on individual triangular elements. Using Eqs. (20) and (23) the expression for the rate of work dissipation becomes

$$D = [v]\sum_{k=1}^{m}(\tau_k cos\delta_k - \sigma_{nk} sin\delta_k)\Delta A_k \tag{24}$$

with normal and tangential stresses σ_{nk} and τ_k found in Eqs. (7) and (8) for given angles δ_k, and m being the number of triangular elements in one quarter of the conical failure surface (in all computations $m > 5000$; for clarity, fewer elements are shown in Fig. 6(b)). Note that stresses σ_{nk} and τ_k are components of stress vector T on the k^{th} triangle, and they are uniquely related to rupture angle δ_k, as illustrated in Fig. 1. Similar to the failure surface being discretized into triangular elements, the volume of the falling block is discretized into tetrahedrons, each with volume ΔV_k

$$\Delta V_k = \frac{1}{6}\left|\left(\vec{p}_k \times \vec{q}_k\right)\cdot\vec{r}_k\right| \tag{25}$$

where $\vec{r}_k$ is shown in Fig. 6(c), and the rate of work done by the weight of one fourth of the conical sections of the failing block is determined from the expression

$$W_\gamma = \gamma\, v \sum_{k=1}^{m}\Delta V_k \tag{26}$$

with γ being the unit weight of rock and v being the magnitude of velocity vector v.

4.2.1. Stability number for quartic cone block with rectangular base

Each of the components in balance Eq. (10) has two terms, one for the conical part of the surface (end sections) and one for the prismatic insert. Substituting the sum of expressions in Eqs. (24) and (A1) for the rate of dissipation and the sum of Eqs. (26) and (A2) for the gravity work (and $W_p = 0$) into balance Eq. (10), and using Eqs. (7) and (8), the following expression for dimensionless group $\sigma_{ci}/\gamma B$ was derived

$$\frac{\sigma_{ci}}{\gamma B} = \frac{\sum_{k=1}^{m}\Delta V_k + \frac{l}{2}\left(\sum_{j=1}^{n} S_j - \frac{B^2}{8}\right)}{B\left(\sum_{k=1}^{m} K_k \Delta A_k + \frac{l}{2}\sum_{j=1}^{n} K_j L_j\right)} \tag{27}$$

where K_k and K_j are given in Eq. (B1) in Appendix B. The stability number is the maximized value of the dimensionless group in Eq. (27), with the geometrical parameters of the failure block being independent variables in the optimization process (Section 5.1).

4.2.2. Factor of safety for quartic cone block with rectangular base

The second stability measure considered is the factor of safety based on the shear strength of the rock, defined in Eq. (12). The Hoek-Brown criterion in its parametric form, reduced by the factor of safety (Fig. 7), is used

$$\sigma_{nd} = \sigma_n = \sigma_{ci}\left\{\left(\frac{1}{m_b} + \frac{sin\delta}{m_b a}\right)\left[\frac{m_b a(1 - sin\delta)}{2sin\delta}\right]^{\frac{1}{1-a}} - \frac{s}{m_b}\right\} \tag{28}$$

$$\tau_d = \frac{\tau}{F} = \frac{\sigma_{ci}}{F}\left\{\frac{cos\delta}{2}\left[\frac{m_b a(1 - sin\delta)}{2sin\delta}\right]^{\frac{a}{1-a}}\right\} \tag{29}$$

The normal stress component is identical to that in Eq. (7), whereas the factored shear stress at failure (shear strength) is reduced by factor of safety F from its full value in Eq. (8). As illustrated in Fig. 7, the relationship of the true rupture angle δ and the factored rupture angle δ_d is

$$\delta = \tan^{-1}(F tan\delta_d) \tag{30}$$

Calculations of the factor of safety require that rates of internal (dissipated) work be calculated based on the factored (reduced) shear strength in Eq. (29) and the rates of the external work in Eq. (10) need to be calculated using the geometry of the failure mechanism based on the reduced rupture angle δ_d rather than rupture angle δ associated with the true strength of the rock.

The work rate terms in Eq. (10) have separate components for the conical part of the failure surface and for the prismatic insert. Substituting expressions in Eqs. (24, 26, A1, A2) and $W_p = 0$ into balance Eq. (10), and using Eqs. (28) and (29), the following implicit equation with respect to the factor of safety was derived

$$\frac{\sigma_{ci}}{\gamma B}\left(\sum_{k=1}^{m} M_k \Delta A_{dk} + \frac{l}{2}\sum_{j=1}^{n} M_j L_{dj}\right) = \frac{1}{B}\left[\sum_{k=1}^{m}\Delta V_{dk} + \frac{l}{2}\left(\sum_{j=1}^{n} S_{dj} - \frac{B^2}{8}\right)\right] \tag{31}$$

where subscript d indicates geometrical quantities (A_{dk}, V_{dk}, L_{dj} and S_{dj}) in the mechanism constructed based on the reduced rupture angle δ_d (Fig. 7, Eq. (30)) and $\sigma_{ci}/\gamma B$ is the dimensionless group describing the rock properties and the cavity geometry. Factor of safety F is embedded in terms M_k and M_j given in Eq. (B2) in Appendix B. Consequently, Eq. (31) is an implicit equation with respect to factor of safety F, and needs to be solved numerically (Section 5.1).

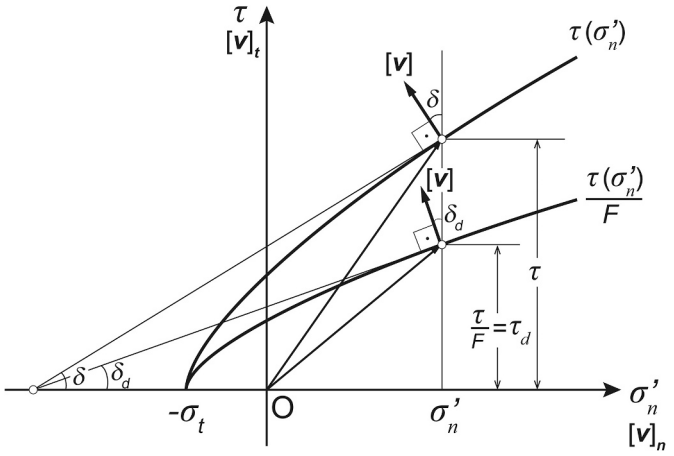

Fig. 7. The Hoek-Brown strength criterion and the strength envelope reduced by factor of safety F.

4.2.3. Support pressure for quartic cone failure block

Cavity roofs that have a small margin of safety may need to be structurally supported to assure a minimum factor of safety required for service. It is considered that the supporting pressure is distributed uniformly on the cavity ceiling, Fig. 3(a, b). The influence of the supporting pressure is included in the last term of the work rate balance in Eq. (10). The supporting pressure is a reaction of the support system to the gravity load, thus its work is negative during failure, and for one quarter of the cone block with a rectangular base (matching the entire ceiling area) it assumes the following form

$$W_p = -\frac{p\, v B(L-l)}{4} \tag{32}$$

For the quadric (elliptic) cone block considered in the next section, the block base area $B(L\text{-}l)$ in Eq. (32) needs to be replaced with the elliptic base area of the block.

Supporting pressure needs to be large enough so that a minimum required value of the factor of safety is maintained. Hoek et al. (2000) suggest that a minimum factor of safety of 1.5–2.0 is acceptable for permanent underground excavations, whereas a value of 1.3 should be required for temporary mine openings. The rates for internal work in Eqs. (24, A1) with stresses in Eqs. (28, 29), external work in Eqs. (26, A2) and the work of the supporting pressure in Eqs. (32, A3) are now substituted into the rate balance in Eq. (10). After some transformation of the resulting equation, the following expression for required (dimensionless) support pressure $p/\gamma B$ is found

$$\frac{p}{\gamma B} = \frac{4}{BL}\left\{\frac{1}{B}\left[\sum_{k=1}^{m}\Delta V_{dk} + \frac{l}{2}\left(\sum_{j=1}^{n} S_{dj} - \frac{B^2}{8}\right)\right] - \frac{\sigma_{ci}}{\gamma B}\left(\sum_{k=1}^{m} M_k\, \Delta A_{dk} + \frac{l}{2}\sum_{j=1}^{n} M_j L_{dj}\right)\right\} \tag{33}$$

where $\sigma_{ci}/\gamma B$ is the value of the dimensionless group for the actual cavity. The supporting pressure is always necessary if the actual dimensionless group $\sigma_{ci}/\gamma B$ is less than its critical value, i.e., stability number N. Factor of safety F in Eq. (33) is embedded in terms M_j and M_k (Eq. (B2)) and it is a given target value of F (e.g., 1.5–2.0). Eq. (33) is an explicit equation that returns the value of dimensionless support pressure $p/\gamma B$ needed to maintain a required value of factor of safety F.

4.3. Elliptic cone block (real quadric cone)

The classical right elliptic cone with height h, or the *real quadric cone*, is expressed in the following algebraic equation

$$\frac{x^2}{a^2} + \frac{y^2}{b^2} = \frac{(z-h)^2}{h^2} \tag{34}$$

with the origin of the coordinate system at the base of the cone (z directed toward the cone apex). This is a special case of the quartic cone in Eq. (13). The cone in Eq. (34) was used to construct the end sections of the block shown in Fig. 2(b). A single elliptic cone as in Eq. (34) has a linear generatrix, and in search for the critical failure block shape, the block was constructed of a series of elliptic cone frusta, each with a different inclination of the generatrix, analogous to the end sections in Fig. 2(a), with the exception that a true elliptic cone does not cover the corners of the cavity ceiling.

Following the steps in Section 4.2, Eq. (34) can be transformed into an equation describing cones contributing j^{th} frustum to the entire cone block

$$x^2 + \frac{y^2}{\lambda^2} = \frac{(z-c_j)^2}{tan^2\alpha_j} \tag{35}$$

where λ is a ratio of the half-axes on the cone base. The block volume is then constructed by a series of elliptic cone frusta defined in Eq. (35), each with different inclination angle of generatrix α_j in cross-section $y = 0$ (plane xOz).

The algebraic form of the classical right elliptic cone in Eq. (34) is simpler than the quartic surface with a rectangular base in Eq. (13), Section 4.2. Considerations of stability follow the steps described in Section 4.2, and they are not repeated here. The same elliptic cone surface was explored earlier in stability analysis of tunnels with circular cross-sections (Park and Michalowski, 2020), and the reader may find the analytical development therein without the Delaunay discretization method useful.

4.4. Rectangular-base pyramid block

A rectangular pyramid block is illustrated in Fig. 2(c) and Fig. 8. The block is constructed with n frusta of rectangular pyramids with decreasing angle of flank inclination, and a matching prismatic insert. The origin of the coordinate system in Fig. 8 is now placed at half-width ($B/2$) below the cavity ceiling, hence the sum of angles η_j is always 45°. Trapezoid-shape failure (or rupture) surfaces with areas A_{xj} and A_{yj} along x- and y-axes (shaded areas in Fig. 8) are inclined to the vertical velocity vector of the block at angles δ_{xj} and δ_{yj}, respectively ($\delta_{xj} = \delta_{yj}$ for a square-base pyramid), defined as

$$\delta_{yj} = \frac{\pi}{2} - \alpha_j \tag{36}$$

$$\delta_{xj} = \frac{\pi}{2} - tan^{-1}\left(\frac{tan\alpha_j}{\lambda}\right) \tag{37}$$

where λ now determines ratio $B/(L-l)$, with L and l being the length of the entire ceiling and the length of the insert, respectively. Areas of failure surfaces A_{xj} and A_{yj}, and the volume of each quarter-frustum V_j are easily determined from the block geometry, and the rate of dissipated work per one quarter of the pyramid is

$$D = \left[v\right]\sum_{j=1}^{n}\left[\left(\tau_{(x)j}cos\delta_{xj} - \sigma_{(x)j}sin\delta_{xj}\right)A_{xj} + \left(\tau_{(y)j}cos\delta_{yj} - \sigma_{(y)j}sin\delta_{yj}\right)A_{yj}\right] \tag{38}$$

where $\sigma_{(x)j}$, $\tau_{(x)j}$ and $\sigma_{(y)j}$, $\tau_{(y)j}$ are found by substituting δ_{xj}, and δ_{yj} (Eqs. (37) and (36)) into Eqs. (7) and (8), respectively. The gravity work rate of one quarter of the pyramidal end sections is

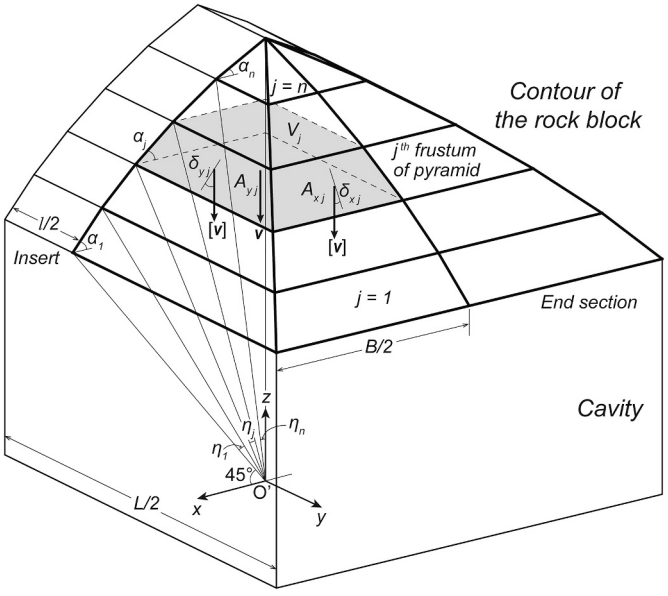

Fig. 8. Half of the failure surface constructed with frusta of rectangular pyramids and a prismatic insert of length l.

$$W_\gamma = \gamma v \sum_{j=1}^{n} V_j \tag{39}$$

with V_j being the volume of one quarter of the j^{th} frustum (shaded volume in Fig. 8). Substituting Eqs. (38), (39), (A1), (A2) and $W_p = 0$ into Eq. (10), and using Eqs. (7) and (8), the dimensionless group $\sigma_{ci}/\gamma B$ is found as

$$\frac{\sigma_{ci}}{\gamma B} = \frac{\sum_{j=1}^{n} V_j + \frac{l}{2}\left(\sum_{j=1}^{n} S_j - \frac{B^2}{8}\right)}{B\sum_{j=1}^{n}\left(K_{xj}A_{xj} + K_{yj}A_{yj} + \frac{l}{2}K_j L_j\right)} \tag{40}$$

where K_j, K_{xj}, and K_{yj} are found from Eq. (B1) in Appendix B after substituting δ_j, δ_{xj}, and δ_{yj}, respectively (compatibility of the pyramid with the prismatic insert requires $\delta_{yj} = \delta_j$). The value of the expression in Eq. (40) maximized with respect to the independent variables (angles η_i, α_i, and ratio λ) is the stability number for the pyramid failure block. The respective expressions for the factor of safety and the supporting pressure can be easily derived following the steps in Section 4.2, and these equations are not presented here. The pyramid-type block is the least complicated shape of those analyzed.

Some aspects of the computations and the results for all three failure mechanisms are discussed in the following section.

5. Results and discussion

5.1. Calculations

The kinematic approach of limit analysis yields the upper bound to factor of safety F and the lower bound to stability number N or to the required support pressure $p/\gamma B$. As the shape of the most critical block in the failure mechanisms is not known a priori, its geometry is sought such that the result is the best bound to the calculated measure of stability. The process of optimization is then carried out, with the independent variables being the parameters describing the block geometry.

All three blocks considered in Section 4 are formed by n conical or pyramidal frusta (and prismatic insert sections), and each of the failure surfaces is described by the same number of independent variables: n angles α_j, n - 1 angles η_j (Fig. 3(a)), and ratio λ of half-axes of conical or pyramidal end sections. Because of the prismatic insert in the block, ratio λ is not equal to the ratio of the ceiling dimensions. Independent of which shape of the block was chosen in Fig. 2 and what stability measure was calculated, the number of independent variables was $2n$ ($n = 10$ was taken in all computations, as increasing the number beyond 10 produced no significant change in the results). The first set of parameters was chosen such that the collapse mechanism was kinematically admissible, and then all angles α_j, η_j and ratio λ were varied to arrive at the best bound to the true solution. The process of optimizing the solution was carried out sequentially in a cycle (loop), changing one variable at a time by one increment. After all variables were adjusted, the cycle was repeated, until the relative difference in the calculated safety measure from one cycle to the next was less than 10^{-6}. All angles were first varied by an increment of 0.1°; this increment was reduced in subsequent cycles to the minimum value of 0.001°. Ratio λ was varied by increments from 0.01 to 0.0001. In the case of the real quadric cone block (Section 4.3), calculations of the work rates in the balance equation were carried out using both the Delaunay discretization method and analytical integration. The difference in results was found to be less than 0.1% when about 5000 of the elements were used in the triangulation method per ¼ of the conical end sections, and that was the number used in all calculations.

For the mechanism with the pyramid block (Fig. 8), calculations with ratio λ varied from frustum to frustum were carried out, but the best solution for all cases calculated were always found when λ was about the same for every frustum.

The optimized solutions indicated that the failing block in all mechanisms always reaches the maximum length and width of the cavity. It should be emphasized that the length of prismatic insert l was not an independent parameter. It is uniquely determined as a difference between given length L of the cavity and the dimension of the cone/pyramid base measured in the y direction (found from the cavity width B and ratio λ).

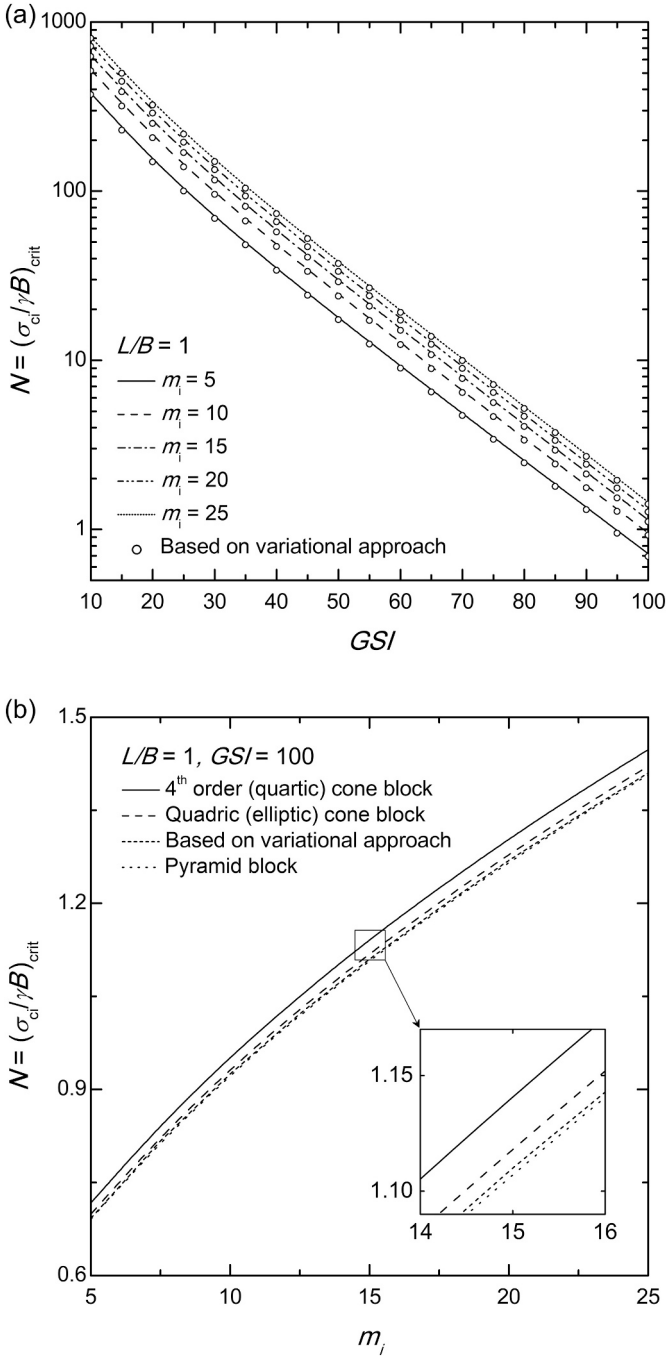

Fig. 9. Stability number N for square-ceiling ($L/B = 1$) cavities: (a) N as a function of GSI for the mechanism with quartic cone block and for the variational approach, and (b) comparison of the stability number for four different failing blocks (all for minimally disturbed rock, $D = 0$).

5.2. Results

5.2.1. Stability number

Stability numbers were calculated from the explicit expression in Eq. (27) for the quartic cone block with a rectangular base and a similar equation developed for the right elliptic (quadric) cone block mechanism; Eq. (40) was used for the pyramid-type failure block.

Calculated stability numbers for square-ceiling cavities are illustrated in Fig. 9(a) as a function of *GSI* (semi-log scale). The lines in the graph represent calculations with the quartic block with prismatic insert. It is surprising that the best (optimized) solution for a square cavity has only two planes of symmetry (no diagonal symmetries). The open-circle bullets are the calculations using the kinematic limit analysis, but with the variational approach in place of the numerical optimization method. The variational approach to roof stability was first suggested by Fraldi and Guarracino (2009) who used it in a series of papers with 2D analysis (Fraldi and Guarracino, 2010, 2011), and it was later utilized by Yang and Huang (2013) for the axi-symmetric case. These papers focused primarily on the shape of the collapsing block. Stability numbers based on the variational approach were calculated by the authors solely for comparative purposes, and, while these results are illustrated in Fig. 9, the details of calculations are not presented here. Perhaps not surprisingly, the results in Fig. 9(a) are very close to one another. So far, however, the variational approach can be reasonably used only for square-ceiling cavities (axi-symmetric solution).

Stability numbers from collapse mechanisms with different block shapes, also for square-ceiling cavities, are shown in Fig. 9(b) as functions of coefficient m_i. The approach yielding the best outcome appears to be the one based on the quartic cone block with insert, followed by the elliptic cone block, whereas the variational approach and the pyramid-type block appear to offer less accuracy, though all these results are within a narrow band of about 5%. While Fig. 9(b) presents comparison of stability numbers, the quartic and quadric mechanisms were also found most critical in calculations of the factor of safety. An increasing stability number with an increase in coefficient m_i is somewhat counterintuitive, though reasonable. A similar observation was the subject of an earlier discussion related to roof stability in tunnels (Park and Michalowski, 2019).

Calculations for square-ceiling cavities lead to an unexpected outcome in that the failing rock block is not symmetric with respect to the two diagonal planes. The best (optimized) solution to the stability number is achieved when the block has a small prismatic insert, as illustrated in Fig. 10(a) and (b). This occurs for the type of blocks schematically illustrated in Fig. 2(a) and (b), but not for the pyramidal block, Fig. 10(c), or the one based on the variational approach, Fig. 10 (d), where the shape is axi-symmetric by definition. This peculiarity was observed in other stability problems, such as the square punch indentation into metals (Shield and Drucker, 1953) and bearing capacity of square footings (Michalowski, 2001). We bring it here only as a curiosity, and will not discuss possible reasons for such an outcome.

More extensive results for the stability number as a function of cavity ceiling aspect ratio L/B are presented in Fig. 11. The first chart illustrates the influence of coefficient m_i in the Hoek-Brown criterion on the stability number. While an increase of N with an increase in L/B is expected, increasing N with increasing m_i is counterintuitive. This was already mentioned in the context of Fig. 9, and it is justifiable based on the discussion of tunnel stability in Park and Michalowski (2019).

The mechanism with the quartic cone block on a rectangular base gives the best solution overall (highest N) when the aspect ratio of the ceiling is close to one (usually, not exceeding 1.7). These results are marked with bold lines in Fig. 11. For larger aspect ratios, it is the elliptic (quadric) cone that yields the best results. The pyramid-shape block failure mechanism was found to give results that are not as good (lower N). The dependence of the stability number on disturbance factor D and on *GSI* is presented in Fig. 11(b) and Fig. 11(c), respectively; they follow an expected trend. For comparative reasons, selected numerical values of the stability number are given in Table 1.

5.2.2. Factor of safety

Factors of safety were calculated from Eq. (31) for the mechanism with a quartic cone block on a rectangular base and from a similar equation developed for a right elliptic cone block. These equations are implicit with respect to the factor of safety, and they require a numerical solution for each set of independent variables during the optimization process. The pyramid-type block mechanism was found to overestimate the factors of safety when compared with the other two mechanisms, and these results are not presented in the paper.

The definition of the factor of safety is that based on the shear strength, given in Eq. (12), with interpretation of the reduced strength illustrated in Fig. 7. Calculated factors of safety are presented in Fig. 12 as a functions of dimensionless group $\sigma_{ci}/\gamma B$, and are based on the mechanism that yields the best results. This is predominantly the 4th order (quartic) cone block on rectangular base shown in Fig. 2(a), and in some cases the elliptic (quadric) cone block in Fig. 2(b). The specific mechanisms are also indicated in Table 2. The factor of safety increases with an increase in group $\sigma_{ci}/\gamma B$ and with an increase in *GSI*. Presented

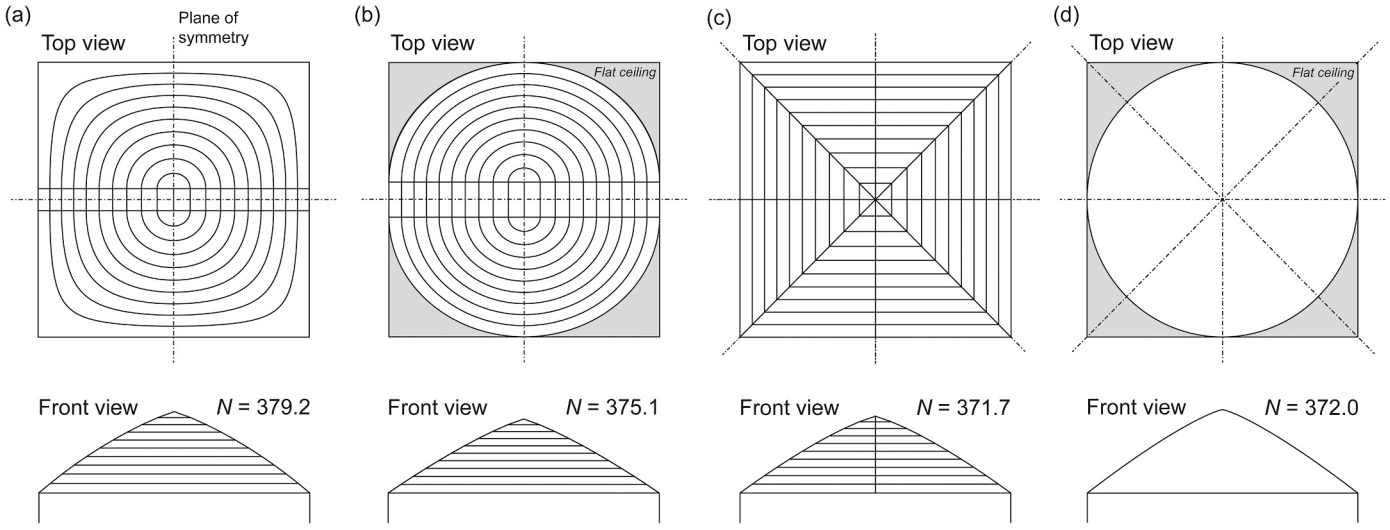

Fig. 10. Top and front views of failure surfaces for square-ceiling cavities, $L/B = 1$ ($m_i = 5$, $D = 0$, $GSI = 10$): (a) quartic cone block on rectangular base with prismatic insert, (b) quadric (elliptic) cone block with insert, (c) a pyramid-type block, and (d) block shape resulting from variational approach (axi-symmetric).

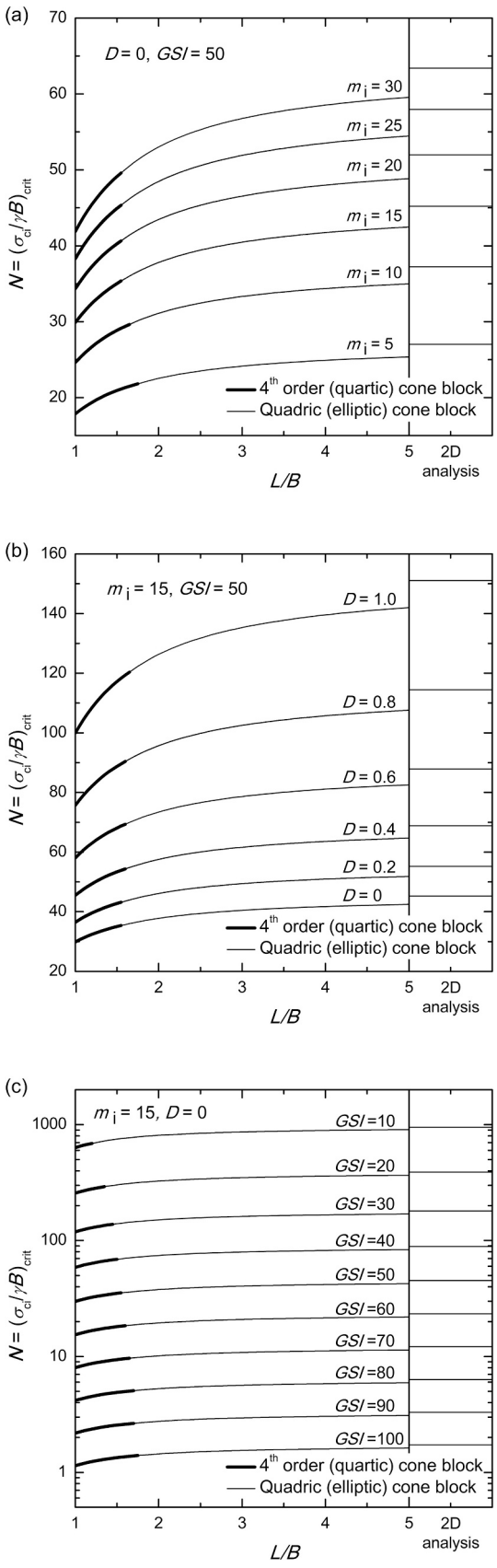

Fig. 11. Stability number for rectangular cavity roofs as a function of length-to-width ratio L/B and for 2D analysis: (a) the influence of coefficient m_i, (b) the influence of disturbance factor D, and (c) the influence of GSI. Results from analysis with quadric (elliptic) cone block mechanism (Section 4.3), except for bold portions of lines presenting results from quartic cone block on rectangular base (Section 4.2).

Table 1
Stability numbers $(\sigma_{ci}/\gamma B)_{crit}$ for flat-ceiling tunnel roofs ($D = 0$).

L/B	m_i	Geological Strength Index *GSI*				
		20	40	60	80	100
1	5	152.40†	34.92†	9.26†	2.55†	0.72†
	15	257.00†	58.72†	15.41†	4.17†	1.14†
	25	330.15†	75.38†	19.72†	5.32†	1.45†
1.5	5	178.88†	40.97†	10.87†	3.00†	0.84†
	15	302.29	68.90†	18.07†	4.89†	1.34†
	25	388.34	88.44†	23.13†	6.24†	1.70†
2	5	193.16	44.13	11.69	3.22	0.90
	15	326.41	74.37	19.48	5.27	1.44
	25	419.29	95.48	24.96	6.73	1.83
3	5	206.79	47.28	12.53	3.45	0.97
	15	349.26	79.63	20.87	5.65	1.54
	25	448.59	102.22	26.73	7.21	1.96
4	5	213.23	48.77	12.93	3.56	1.00
	15	360.05	82.12	21.52	5.83	1.59
	25	462.43	105.41	27.57	7.43	2.02
5	5	216.96	49.64	13.16	3.63	1.02
	15	366.30	83.56	21.90	5.93	1.62
	25	470.45	107.26	28.05	7.57	2.06
2D analysis	5	230.44	52.85	14.02	3.87	1.09
	15	388.85	88.93	23.32	6.31	1.73
	25	499.36	114.14	29.86	8.05	2.19

† Mechanism with 4th order (quartic) cone block on rectangular base, all other results either 2D or based on elliptic (quadric) cone block

in semi-log scale, the factors of safety for different aspect ratios of the cavity ceiling L/B fit in a relatively narrow band. The computational results are shown for L/B equal to 1, 1.5, 2, 4, and for plane-strain analysis. For comparative purposes, numerical values of F for selected cases are given in Table 2.

Calculations of the factor of safety based on the rock shear strength are intricate, because the Hoek-Brown criterion is a function of principal stresses, and it does not have an explicit form presenting the shear strength envelope as a function of normal stress. Therefore, the parametric form of the Hoek-Brown criterion in Eqs. (7) and (8) was used.

The factor of safety is often defined based on compressive strength of intact rock σ_{ci}. The sole reason for such a definition is the simplicity of calculations. In general, however, factors of safety so defined significantly overestimate those based on the shear strength. This issue was discussed earlier in the context of slopes (Michalowski and Park, 2020). It is a peculiarity, however, that for cavities with flat ceilings the two definitions yield an identical value of the safety factor. However, this is not true for curved-ceiling cavities, and the analytical justification in the context of 2D analysis was discussed in Park and Michalowski (2019).

5.2.3. *Supporting pressure*

Cavities and tunnels utilized as part of underground infrastructure require a minimum factor of safety (typically, around 2.0) to be met during their service time. For the quartic cone block on a rectangular base, the supporting pressure was calculated from the explicit expression in Eq. (33) and a similar equation was developed for the elliptic (quadric) cone mechanism. The best bounds to the required supporting pressure are presented in Fig. 13 in three log-log charts, each for a different given factor of safety F: 1, 1.5 and 2 (defined as in Eq. (12)). The supporting pressure in Figs. 13(b) and 13(c) assure that the given factor 1.5 or 2.0, respectively, will be maintained. The plots include the more critical results of the two conical block mechanisms in Figs. 2(a) and 2(b). A more specific indication of the critical mechanisms for specific cases is included in Tables 3 and 4. Dimensionless pressure $p/\gamma B$ (see Fig. 3 for p) is shown as a function of dimensionless group $\sigma_{ci}/\gamma B$ for *GSI* in the range of 20 to 100. The pressure is given for a ceiling aspect ratio of 1 (square), 2 and for a long cavity (plane-strain analysis).

The trends of the solution are what one would expect: the larger the rock strength ($\sigma_{ci}/\gamma B$), the lower the support pressure needed; the larger the ceiling aspect ratio, the larger the support pressure needed, and the

Table 2
Factors of safety F for flat-ceiling roofs ($D = 0$).

$\sigma_{ci}/\gamma B$	*GSI*	m_i	L/B			
			1	1.5	2	2D analysis
500	20	5	3.33†	2.80†	2.59	2.17
		15	1.97†	1.65	1.53	1.28
		25	1.53†	1.29	1.19	1.00
100	40	5	2.92†	2.45†	2.27	1.89
		15	1.73†	1.45†	1.34	1.12
		25	1.35†	1.13†	1.05	0.88
20	60	5	2.20†	1.85†	1.71	1.43
		15	1.32†	1.11†	1.03	0.86
		25	1.03†	0.87†	0.80	0.67
10	80	5	4.01†	3.37†	3.11	2.59
		15	2.44†	2.05†	1.90	1.58
		25	1.91†	1.61†	1.49	1.24
2	100	5	2.86†	2.40†	2.22	1.84
		15	1.79†	1.50†	1.39	1.16
		25	1.41†	1.18†	1.09	0.91

† Mechanism with 4th order (quartic) cone block on rectangular base, all other results either 2D or based on elliptic (quadric) cone block.

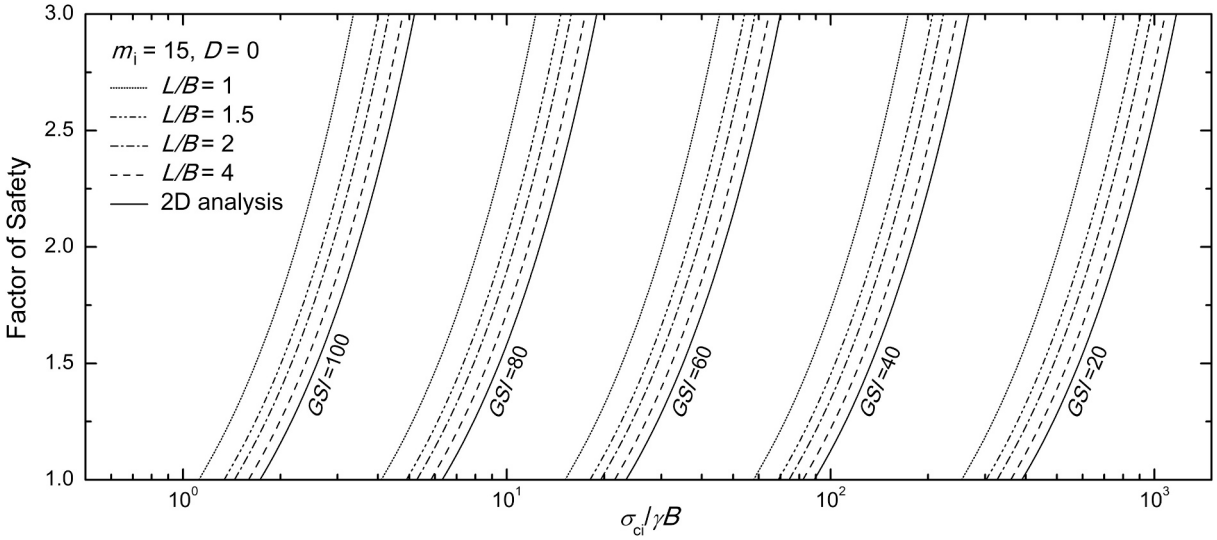

Fig. 12. Factors of safety as functions of dimensionless group $\sigma_{ci}/\gamma B$ for square and rectangular-ceiling, and long cavities such as tunnels (plane strain analysis).

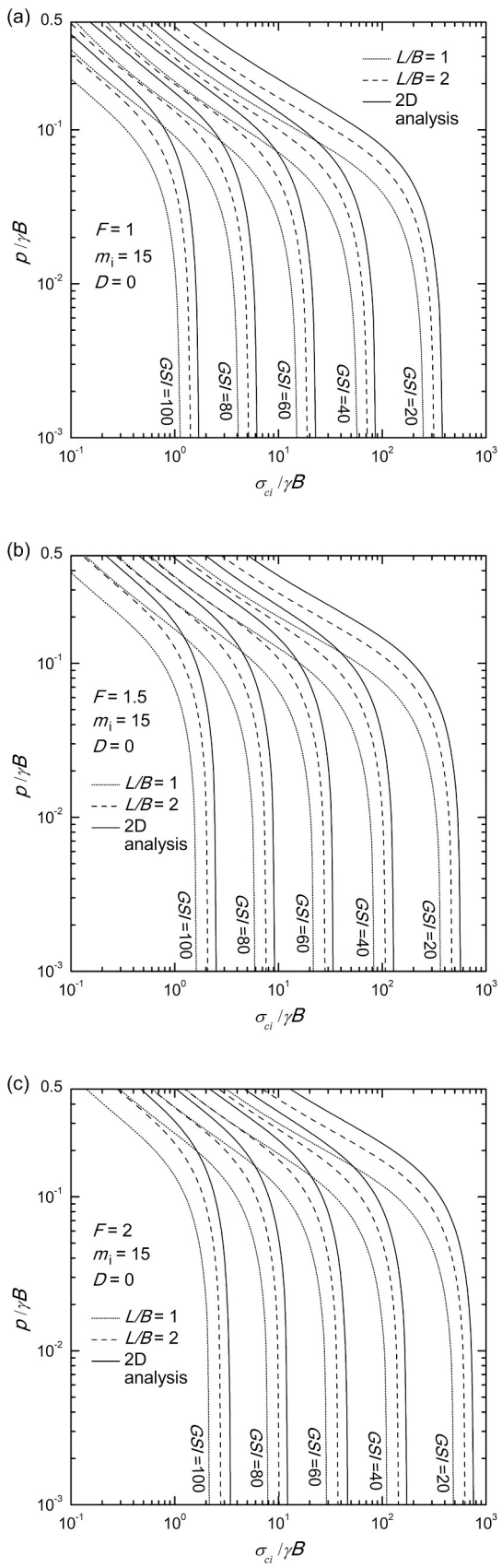

Fig. 13. Required supporting pressure $p/\gamma B$: (a) pressure required for limit equilibrium (factor of safety $F = 1$), (b) pressure required to meet target factor of safety $F = 1.5$, and (c) required pressure to maintain $F = 2.0$.

Table 3
Required supporting pressure $p/\gamma B \times 10^3$ for flat-ceiling roofs assuring limit equilibrium ($D = 0$).

$\sigma_{ci}/\gamma B$	*GSI*	m_i	*L/B*			
			1	1.5	2	2D analysis
		5	36.08†	56.16†	67.30	98.70
100	20	15	39.11†	52.10	59.35	79.23
		25	35.98†	46.76	52.72	69.03
		5*	–	–	–	–
50	40	15	8.66†	19.39†	25.32	42.01
		25	15.78†	24.68†	29.67	43.52
		5	-*	11.97†	23.60	58.84
10	60	15	25.92†	40.10†	47.86	70.26
		25	29.26†	41.01†	47.48	65.94
		5	36.81†	69.08†	86.25†	139.24
2	80	15	51.17†	71.08†	81.74	113.73
		25	49.03†	65.31†	74.14	100.03
		5*	–	–	–	–
1	100	15	13.32†	33.05†	43.61	75.31
		25	26.18†	42.33†	51.08	76.76

† Mechanism with 4th order (quartic) cone block on rectangular base, all other results either 2D or based on elliptic (quadric) cone block.
* No supporting pressure required.

Table 4
Required supporting pressure $p/\gamma B \times 10^3$ for flat-ceiling roofs assuring factor of safety $F = 2$ ($D = 0$).

$\sigma_{ci}/\gamma B$	*GSI*	m_i	*L/B*			
			1	1.5	2	2D analysis
		5	165.41†	217.32†	245.38	327.92
100	20	15	121.21†	153.79	172.05	222.49
		25	100.72†	130.26	145.16	186.15
		5	62.52†	104.61†	127.23	194.70
50	40	15	77.30†	104.65†	119.76	162.72
		25	72.42†	93.95†	108.05	143.44
		5	134.02†	193.16†	224.43†	321.31
10	60	15	117.76†	154.75†	174.70	233.87
		25	105.02†	135.38†	151.95	200.06
		5	254.40†	346.77†	396.33†	551.64
2	80	15	181.87†	235.36†	263.60†	350.94
		25	154.55†	197.96†	220.78	290.21
		5	139.25†	230.53†	279.49	432.89
1	100	15	142.84†	195.84†	223.81	310.33
		25	130.74†	173.84†	196.50	265.33

† Mechanism with 4th order (quartic) cone block on rectangular base, all other results either 2D or based on elliptic (quadric) cone block.

larger the *GSI*, the lower the pressure needed. If the curve for a given cavity and for required factor of safety F in Fig. 13 intersects the abscissa at $\sigma_{ci}/\gamma B$ equal to stability number N for this cavity, then only a small support pressure of $p/\gamma B = 10^{-3}$ is needed to maintain the required F. If the stability number is substantially larger than dimensionless group $\sigma_{ci}/\gamma B$ marked on the abscissa, the cavity roof does not need a support pressure to maintain the selected factor of safety. Numerical values of the supporting pressure for selected cases are given in Tables 3 and 4.

5.3. Other quartic surfaces considered in the analysis

In addition to the quartic cone block on a rectangular base and the real quadric (elliptic) cones considered in Sections 4.2 and 4.3, three other quartic surfaces were considered. All of them are special cases of 4th order surfaces, constructed through addition of higher-order term $x^2y^2/(a^2b^2)$ to (or subtraction from) equations of quadric surfaces in order to allow for a rectangular base of the rock block. These surfaces are: modified hyperboloid of two sheets, modified elliptic paraboloid, and modified ellipsoid (dome), all illustrated in Fig. 14 and defined in Eqs. (41)–(43)

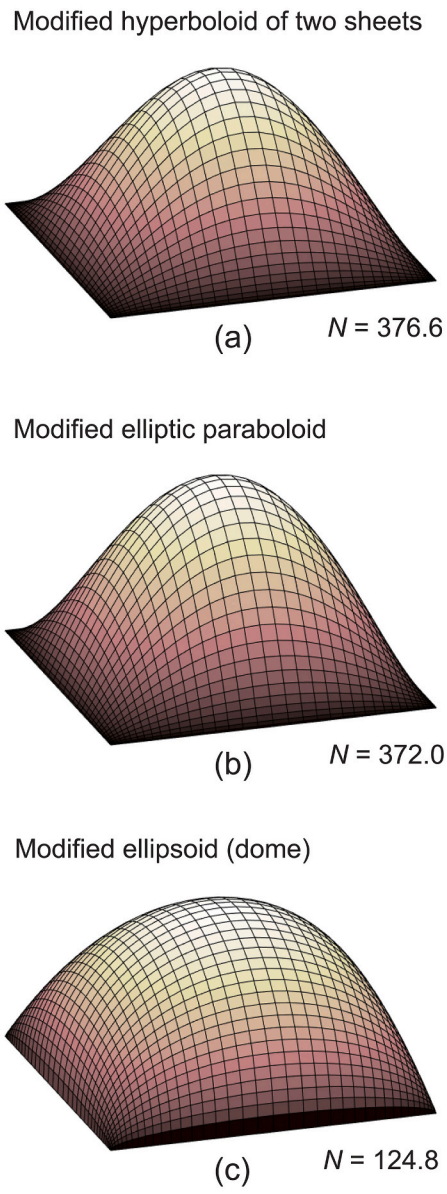

Fig. 14. Other higher-order surfaces (quartics) considered in the analysis ($L/B = 1$, $m_i = 5$, $D = 0$, $GSI = 10$): (a) modified hyperbola of two sheets, (b) modified elliptic paraboloid, and (c) modified ellipsoid (dome). (For interpretation of the references to colour in this figure legend, the reader is referred to the web version of this article.)

Modified hyperboloid of two sheets:

$$-\frac{x^2}{a^2}-\frac{y^2}{b^2}+\frac{z^2}{c^2}+\frac{x^2}{a^2}\frac{y^2}{b^2}=1 \tag{41}$$

Modified elliptic paraboloid:

$$\frac{x^2}{a^2}+\frac{y^2}{b^2}-\frac{x^2}{a^2}\frac{y^2}{b^2}=\frac{z}{c} \tag{42}$$

Modified ellipsoid (dome) :

$$\frac{x^2}{a^2}+\frac{y^2}{b^2}+\frac{z^2}{c^2}-\frac{x^2}{a^2}\frac{y^2}{b^2}=1 \tag{43}$$

where *a, b, c* are constants in the equations defining the specific shape, but they were made variable in search for the most critical shape. These surfaces have a nonlinear generatrix, and each block was defined by a single equation, rather than formed of separate frusta. The Delaunay triangulation method was used in calculations of work rates of internal and external forces. The surface in Eq. (43) was considered earlier by Korotkiy et al. (2015) as an example of computer geometric modeling.

Stability numbers for all three blocks over a square cavity are included in Fig. 14. The modified hyperboloid of two sheets was found to be the most critical block shape of the three, but still, not as critical as the square-base quartic block in Fig. 10(a). However, both the modified hyperboloid of two sheets and the elliptic paraboloid are competitive with the blocks considered earlier (Fig. 9 and Fig. 10). The modified ellipsoid (dome) block seems to be an outlier, which underestimates the stability number calculated with the quartic (elliptic) cone on a rectangular base (Section 4.2) by more than 60%. Indeed the dome block is a very stable configuration, and the failure governed by any of the other block shapes considered would occur well before the dome block would become vulnerable to collapse.

5.4. Remarks on the use of the parametric form of the Hoek-Brown strength criterion

The Hoek-Brown failure criterion is a function of major and minor principal stresses, while some methods, including limit analysis, call for an explicit representation of the shear strength as a function of the normal stress on kinematic discontinuities (failure surfaces). For that reason Hoek and Brown suggested a substitution function in a form similar to the following expression (Hoek and Brown, 1980)

$$\tau = A\sigma_{ci}\left(\frac{\sigma_n' + \sigma_t}{\sigma_{ci}}\right)^B \tag{44}$$

where τ and σ_n' are the components of the stress vector on the strength envelope, σ_{ci} is the compressive strength of the intact rock, σ_t is the tensile strength, and A and B are dimensionless material parameters. If the parameters in the Hoek-Brown criterion, Eq. (1), are known, then parameters A and B in expression (44) can be estimated for a given range of stresses. Consequently, kinematic limit analysis of stability of a roof cavity or a slope will yield very similar results when using either of the two criteria. This was confirmed with the outcome of calculations of the stability number for square-ceiling roofs presented in Fig. 9(a). The lines in that chart were found from the analysis based on the parametric form of the Hoek-Brown criterion in Eqs. (7) and (8), whereas the open bullets are from the approach with the strength criterion in Eq. (44). These results are nearly identical (the kinematic approach yields the lower bound to the stability number).

The shape of a failure block in a roof collapse mechanism in tunnels was determined by Fraldi and Guarracino (2009) using the variational approach and the strength criterion in Eq. (44). This shape was independently determined using the parametric form of the Hoek-Brown criterion, and the two contours were found to be identical (Park and Michalowski, 2019). It is reasonable to conclude that the accuracy of calculations is comparable, whether the parametric form of the Hoek-Brown criterion is used or the substitution function is employed (i.e., the quantitative results are very close, if not identical). The authors found it convenient to use the parametric form of the Hoek-Brown criterion, because of evading the fitting process for finding parameters A and B in Eq. (44). On the other hand, Eq. (44) may be easier to handle in the analysis, because of its relatively simple form.

The third method often exercised when using limit analysis with nonlinear strength criteria calls for linearizing the strength envelope, the method introduced into kinematic limit analysis by Drescher and Christopoulos (1988). Both former methods are more accurate than the latter. Calculations of stability numbers for square-ceiling cavities in this paper were underestimated by the method with linearized strength criterion by 6%, while the difference increased to 8% for the plane-strain analysis. The difference was found in a similar range in the analyses of slope stability (Michalowski and Park, 2020), with a larger difference for

the steeper slopes. It is surprising that this difference is not larger, considering that the linearization of the strength criterion is a rather crude tool.

6. Conclusions

This study was devoted to quantitative assessment of safety of underground cavities in rock against roof collapse. The following are the conclusions derived from the study.

1. Even though the roof collapse mechanism in the form of one block seems fairly uncomplicated, the analysis was found to be quite intricate. The block shapes that yield the best estimates of the safety measures are the 4th order (quartic) conical surface block and the 2nd order (quadric) elliptic cone. Enriched with a prismatic insert, they were found to fit the cavities with any ceiling aspect ratio well.
2. Numerical generation of a rock block shape, while a feasible option for geomaterials described with a linear shear strength envelope, was found less attractive when tried for the Hoek-Brown strength criterion. This is the outcome of the normality flow rule used in limit analysis and multiplicity of the rupture angles when using nonlinear strength envelopes.
3. Analytical complexity of the 4th order surfaces makes it challenging to develop explicit expressions for the rates of work in the collapse mechanism. It was found convenient to use a numerical procedure based on the Delaunay triangulation method to integrate both the rate of internal work along the failure surfaces and the work rate of the rock weight.
4. As for cavities with rectangular ceilings, the best estimates of the safety measures for square-ceiling cavities were found for blocks with quartic (4th order) cone blocks. It was found peculiar, however, that the shape of failure blocks associated with the most critical failure mechanisms in square-ceiling cavities was not characterized by diagonal symmetry planes. These critical mechanisms included a narrow prismatic insert.
5. When applied in rock engineering, the factor of safety is often defined by factoring the uniaxial compressive strength of intact rock, rather than the shear strength. The two definitions typically yield different values for the same problem; for example, for the circular cross-section tunnels the factor of safety based on compressive strength grossly overestimates the factor based on the shear strength. It was unexpected to find out in this study that the two definitions yield the same value of the safety factor when applied to the problem of roof collapse in flat-ceiling cavities. This is the consequence of the ceiling geometry.
6. The original Hoek-Brown criterion is a function of the major and minor principal stresses, whereas some methods for stability assessment, including the kinematic limit analysis, require an explicit representation of the rock shear strength as a function of the normal stress on the failure surface. The authors found it convenient to use a method with the parametric representation of the Hoek-Brown criterion in place of a substitution function with the shear strength explicitly dependent on the normal stress on the failure surface.

Declaration of Competing Interest

The authors declare that they have no known competing financial interests or personal relationships that could have appeared to influence the work reported in this paper.

Acknowledgements

The work presented in this paper was carried out while the authors were supported by the National Science Foundation, Grant No. CMMI-1901582 and the Horace Rackham School of Graduate Studies at the University of Michigan. The work was also supported by the National Research Foundation of Korea (NRF) grant funded by the Korea government (MSIT), No. 2021R1G1A1003943. This support is greatly appreciated.

Appendix A

A.1. Prismatic insert

The rate of work dissipation in one quarter of the prismatic insert during the roof collapse is determined by summing up the rates on rupture surfaces of every j^{th} element of the block

$$D = \frac{l\,[v]}{2}\sum_{j=1}^{n}\left(\tau_j cos\delta_j - \sigma_{nj} sin\delta_j\right)L_j \tag{A1}$$

where l is the length of the insert, and L_j is the length of j^{th} rupture surface B_jB_{j+1} as in Fig. 3(a). The rate of gravity work of one quarter of the insert is

$$W_\gamma = \gamma\, v\frac{l}{2}\left(\sum_{j=1}^{n} S_j - \frac{B^2}{8}\right) \tag{A2}$$

with S_j being the area of j^{th} triangle OB_jB_{j+1} in Fig. 3(a). The rate of work of the supporting pressure per one quarter of the insert is

$$W_p = -\frac{p\, v Bl}{4} \tag{A3}$$

Appendix B

B.1. Common expressions

$$K_j = \frac{cos^2\delta_j}{2}\left[\frac{m_b a\left(1-sin\delta_j\right)}{2sin\delta_j}\right]^{\frac{a}{1-a}} - \left[\left(\frac{1}{m_b}+\frac{sin\delta_j}{m_b a}\right)\left(\frac{m_b a\left(1-sin\delta_j\right)}{2sin\delta_j}\right)^{\frac{1}{1-a}} - \frac{s}{m_b}\right] sin\delta_j \tag{B1}$$

Rupture angles δ_{xj} and δ_{yj} need to be substituted in Eq. (B1) when used in the first and second term in the sum of the denominator in Eq. (40).

$$M_j = \frac{cos\delta_j}{2F}\left[\frac{m_b a\left(1-sin\delta_j\right)}{2sin\delta_j}\right]^{\frac{a}{1-a}} cos\delta_{dj} - \left[\left(\frac{1}{m_b}+\frac{sin\delta_j}{m_b a}\right)\left(\frac{m_b a\left(1-sin\delta_j\right)}{2sin\delta_j}\right)^{\frac{1}{1-a}} - \frac{s}{m_b}\right] sin\delta_{dj} \tag{B2}$$

where $\delta_j = \tan^{-1}(F \tan \delta_{dj})$. When $F = 1$, M_j in Eq. (B2) becomes identical to K_j in Eq. (B1).

References

Balmer, G., 1952. A general analysis solution for Mohr's envelope. Proc. ASTM. 52, 1260–1271.

Barton, N., 1976. The shear strength of rock and rock joints. Int. J. Rock Mech. Min. Sci. Geomech. Abstr. 13, 255–279. https://doi.org/10.1016/0148-9062(76)90003-6.

Bieniawski, Z.T., 1974. Estimating the strength of rock materials. J. South. Afr. Inst. Min. Metall. 74, 312–320.

Chen, W.F., 1975. Limit Analysis and Soil Plasticity. Elsevier, New York.

Chen, W.F., Drucker, D.C., 1969. Bearing capacity of concrete blocks or rock. J. Eng. Mech. Div. 95, 955–978. https://doi.org/10.1061/JMCEA3.0001149.

Delaunay, B., 1934. Sur La Sphere Vide. Bulletin de l'Académie des Sciences de l'URSS, Classe des Sciences Mathématiques et Naturelles. 6, 793–800.

Drescher, A., Christopoulos, C., 1988. Limit analysis slope stability with nonlinear yield condition. Int. J. Num. Analyt. Meth. Geomech. 12 (3), 341–345.

Drucker, D., Prager, W., Greenberg, H., 1952. Extended limit design theorems for continuous media. Q. Appl. Math. 9, 381–389. https://doi.org/10.1090/qam/45573.

Fraldi, M., Guarracino, F., 2009. Limit analysis of collapse mechanisms in cavities and tunnels according to the Hoek–Brown failure criterion. Int. J. Rock Mech. Min. Sci. 46, 665–673. https://doi.org/10.1016/j.ijrmms.2008.09.014.

Fraldi, M., Guarracino, F., 2010. Analytical solutions for collapse mechanisms in tunnels with arbitrary cross sections. Int. J. Solids Struct. 47, 216–223. https://doi.org/10.1016/j.ijsolstr.2009.09.028.

Fraldi, M., Guarracino, F., 2011. Evaluation of impending collapse in circular tunnels by analytical and numerical approaches. Tunn. Undergr. Space Technol. 26, 507–516. https://doi.org/10.1016/j.tust.2011.03.003.

Hoek, E., Brown, E.T., 1980. Empirical strength criterion for rock masses. J. Geot. Eng. Div. 106, 1013–1035. https://doi.org/10.1061/AJGEB6.0001029.

Hoek, E., Brown, E.T., 2019. The Hoek–Brown failure criterion and GSI–2018 edition. J. Rock Mech. Geotech. Eng. 11, 445–463. https://doi.org/10.1016/j.jrmge.2018.08.001.

Hoek, E., Marinos, P., 2007. A brief history of the development of the Hoek-Brown failure criterion. Soils Rocks. 2, 2–13.

Hoek, E., Kaiser, P.K., Bawden, W.F., 2000. Support of Underground Excavations in Hard Rock. CRC Press.

Hoek, E., Carranza-Torres, C., Corkum, B., 2002. Hoek-Brown failure criterion - 2002 edition. Proceedings of NARMS-Tac. 1, 267–273.

Huang, F., Yang, X., Ling, T., 2014. Prediction of collapsing region above deep spherical cavity roof under axis-symmetrical conditions. Rock Mech. Rock. Eng. 47, 1511–1516. https://doi.org/10.1007/s00603-013-0455-y.

Korotkiy, V., Usmanova, E., Khmarova, L., 2015. Surface as an object of computer geometric modelling. Procedia Eng. 129, 775–780. https://doi.org/10.1016/j.proeng.2015.12.103.

Kumar, P., 1998. Shear failure envelope of Hoek-Brown criterion for rockmass. Tunn. Undergr. Space Technol. 13, 453–458. https://doi.org/10.1016/S0886-7798(98)00088-1.

Leca, E., Dormieux, L., 1990. Upper and lower bound solutions for the face stability of shallow circular tunnels in frictional material. Géotechnique. 40, 581–606. https://doi.org/10.1680/geot.1990.40.4.581.

Li, A., Merifield, R., Lyamin, A., 2008. Stability charts for rock slopes based on the Hoek–Brown failure criterion. Int. J. Rock Mech. Min. Sci. 45, 689–700. https://doi.org/10.1016/j.ijrmms.2007.08.010.

Lippmann, H., 1971. Plasticity in rock mechanics. Int. J. Mech. Sci. 13, 291–297. https://doi.org/10.1016/0020-7403(71)90054-3.

Michalowski, R.L., 1985. Limit analysis of quasi-static pyramidal indentation of rock. Int. J. Rock Mech. Min. Sci. Geomech. Abstr. 22, 31–38. https://doi.org/10.1016/0148-9062(85)92591-4.

Michalowski, R.L., 2001. Upper-bound load estimates on square and rectangular footings. Géotechnique. 51, 787–798. https://doi.org/10.1680/geot.2001.51.9.787.

Michalowski, R.L., Park, D., 2020. Stability assessment of slopes in rock governed by the Hoek-Brown strength criterion. Int. J. Rock Mech. Min. Sci. 127, 104217 https://doi.org/10.1016/j.ijrmms.2020.104217.

Mollon, G., Dias, D., Soubra, A.H., 2011. Rotational failure mechanisms for the face stability analysis of tunnels driven by a pressurized shield. Int. J. Numer. Anal. Methods Geomech. 35, 1363–1388. https://doi.org/10.1016/j.jrmge.2021.10.006.

Park, D., Michalowski, R.L., 2017. Three-dimensional stability analysis of slopes in hard soil/soft rock with tensile strength cut-off. Eng. Geol. 229, 73–84. https://doi.org/10.1016/j.enggeo.2017.09.018.

Park, D., Michalowski, R.L., 2018. Tunnel Roof Stability in Soft Rock with Tension Cutoff. In: GeoShanghai International Conference, 361-368. Springer. https://doi.org/10.1007/978-981-13-0017-2_36.

Park, D., Michalowski, R.L., 2019. Roof stability in deep rock tunnels. Int. J. Rock Mech. Min. Sci. 124, 104139 https://doi.org/10.1016/j.ijrmms.2019.104139.

Park, D., Michalowski, R.L., 2020. Three-dimensional roof collapse analysis in circular tunnels in rock. Int. J. Rock Mech. Min. Sci. 128, 104275 https://doi.org/10.1016/j.ijrmms.2020.104275.

Park, D., Michalowski, R.L., 2021. Three-dimensional stability assessment of slopes in intact rock governed by the Hoek-Brown failure criterion. Int. J. Rock Mech. Min. Sci. 137, 104522 https://doi.org/10.1016/j.ijrmms.2020.104522.

Paul, B., 1961. A Modification of the Coulomb-Mohr Theory of Fracture, 28, pp. 259–268. https://doi.org/10.1115/1.3641665.

Shield, R., Drucker, D.C., 1953. The application of limit analysis to punch-indentation problems. J. Appl. Mech. 20, 453–460. https://doi.org/10.1115/1.4010747.

Sloan, S., Assadi, A., 1992. Stability of shallow tunnels in soft ground. In: Predictive soil mechanics: Proceedings of the Wroth Memorial Symposium held at St Catherine's College, Oxford, 27–29 July 1992. Thomas Telford Publishing, pp. 644–663.

Suchowerska, A.M., Merifield, R.S., Carter, J.P., Clausen, J., 2012. Prediction of underground cavity roof collapse using the Hoek–Brown failure criterion. Comput. Geotech. 44, 93–103. https://doi.org/10.1016/j.compgeo.2012.03.014.

Taylor, D.W., 1937. Stability of earth slopes. J. Boston Soc. Civil Engineers. 24, 197–247.

Yang, X., Huang, F., 2013. Three-dimensional failure mechanism of a rectangular cavity in a Hoek–Brown rock medium. Int. J. Rock Mech. Min. Sci. 61, 189–195. https://doi.org/10.1016/j.ijrmms.2013.02.014.